Volume 22
Number 2
14 January 2026
Pages 261–556

Soft Matter

rsc.li/soft-matter-journal

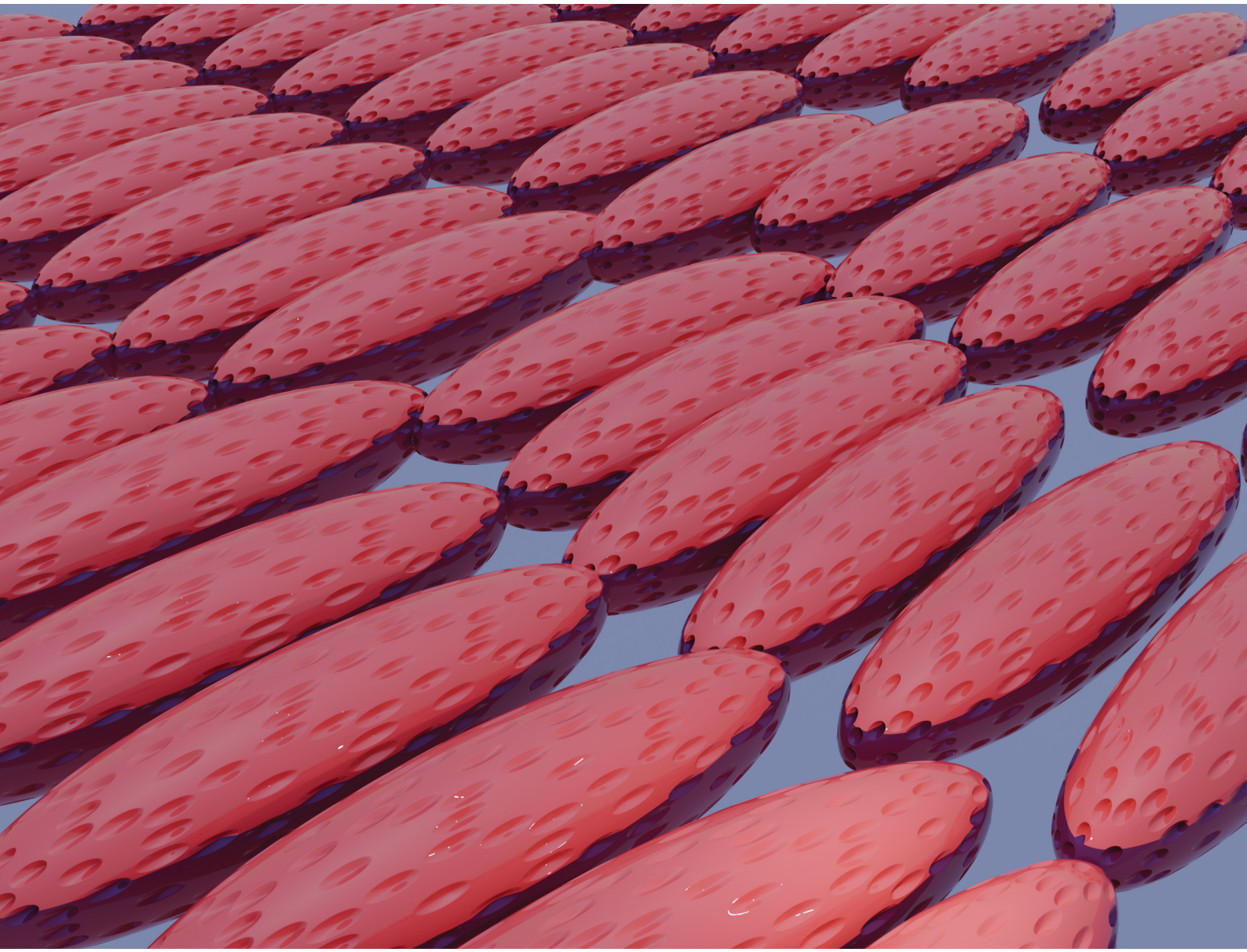

ISSN 1744-6848

ROYAL SOCIETY OF CHEMISTRY

PAPER

Md Anisur Rahman and Peter J. Beltramo
Controlling self-assembly and interfacial mechanics of polymer spheres and ellipsoids at fluid interfaces with surface roughness

Soft Matter

ROYAL SOCIETY OF CHEMISTRY

PAPER

View Article Online
View Journal | View Issue

Cite this: *Soft Matter*, 2026, **22**, 315

Controlling self-assembly and interfacial mechanics of polymer spheres and ellipsoids at fluid interfaces with surface roughness

Md Anisur Rahman and Peter J. Beltramo *

In this study, we describe the effect of surface topography on monolayer assembly and mechanics of spherical and ellipsoidal colloids at an air–water interface. Building off our prior work which directly measured the roughness-dependent capillary pinning of individual particles, we now show how the reduction in capillary interaction energy between rough ellipsoids, and the increase in interaction energy between spheres, impacts their collective assembly. Two types of surface topography (convex/concave) and two degrees of roughness are compared with their smooth analogues. With increasing roughness, the measured surface pressure increases for spheres, in accordance with stronger capillary interactions, and decreases in ellipsoids, confirming that individual particle attributes impact their monolayer properties. However, the type of surface topography, not just the roughness magnitude, is shown to be a critical aspect of the assembly morphology as the interfaces approach their jammed state. In particular, concave rough ellipsoids are observed to form a complete unidirectional monolayer with high area fraction ($\sim$0.86), avoiding the kinetically arrested assemblies and low area fraction jamming (0.68) shown by smooth ellipsoids. Moreover, monolayers of concave rough ellipsoids demonstrate a two-dimensional interfacial isotropic–nematic phase transition with increasing particle areal density. The surface topography mediated capillary pinning and wetting behavior, coupled with the altered interparticle interactions and the resultant interfacial microstructure, further dictates the monolayer's ability to resist compressive deformation and collapse mechanics. These findings open up opportunities to realize complex two-dimensional (2D) ordered microstructures from anisotropic particles and manipulate fluid–fluid interface stability in emulsions and foams by leveraging particle topography and shape engineering.

Received 4th September 2025,
Accepted 18th November 2025

DOI: 10.1039/d5sm00903k

rsc.li/soft-matter-journal

Introduction

The unique properties of colloids pinned to fluid interfaces can be leveraged to mechanically stabilize fluid interfaces for Pickering emulsions,[1–4] bijels,[5,6] and foams,[7] and also for the bottom-up assembly of 2D micro-/nanopatterned surfaces with applications in photonics,[8] phononics,[9] biosensing and bioengineering,[10,11] antireflective and superhydrophobic coatings,[12–14] solar cells,[15–18] and micro-lens arrays.[19,20] At a fundamental level, micron-scale colloidal particles are also an excellent model system for studying phase transitions since the structures and dynamics of individual particles can be directly monitored in real time *via* optical microscopy.[21,22] Such diverse applications have spurred an immense interest in studying particle-laden interfaces, and necessitate an understanding of how a single particle pins to the interface, interacts with its neighbors, and assembles into a monolayer with the requisite microstructure and/or mechanical stability.

The interfacial microstructure of colloids at fluid interfaces is generally dictated by the combination of interparticle electrostatic repulsion and capillary attraction. Monodisperse smooth polymer microspheres are easy to synthesize in large quantities and exhibit dominant isotropic electrostatic repulsion,[23–26] causing hexagonal packing with spacing tuned by the aqueous electrolyte concentration.[23,27,28] These ordered particulate monolayers can be transferred to a flat substrate by Langmuir–Blodgett deposition, where they can subsequently serve as a mask in nanosphere lithography (NSL) to form symmetric metal and/or dielectric nanoarray patterns in the interstitial space between particles to generate plasmonic devices.[29] NSL offers a more scalable approach than direct-write processes, but only high-fidelity hexagonal ordering is possible from dipolar spheres. However, recent simulations and experimental results suggest that anisotropically ordered nanoscale plasmonic arrays possess increased signal-to-noise ratios desirable for next-generation photocatalysis or biosensing technologies.[30]

Department of Chemical Engineering, University of Massachusetts Amherst, Amherst, Massachusetts 01003, USA. E-mail: pbeltramo@umass.edu

Therefore, to access a wider range of ordered interfacial microstructures, it is imperative to introduce directional interactions into the system.[31] Such anisotropic interactions between particles can be invoked by using anisotropic particles, external electric or magnetic fields,[32] interfacial curvature gradients,[33,34] or by immersing isotropic particles in a template anisotropic fluid.[35] At the particle level, directional quadrupolar capillary interactions can arise from shape anisotropy, such as in ellipsoids.[36] Non-constant curvature of the ellipsoid necessitates a curved meniscus, rising at the sides and dipping at the tips, to maintain a constant three-phase contact angle, θ_c, according to Young's law.[37] A similar quadrupolar deformation also results from roughness induced nanoscale contact line undulations around spherical particles.[38] Regardless of the origin, distortions in interfacial contact lines give rise to excess interfacial area and thus raise the interfacial free energy, minimization of which causes capillary attraction between the particles.

Although this force is directionally dependent, it is so strong (several orders of magnitude greater than thermal energy) that particles tend to form kinetically arrested multiparticle aggregates at fluid interfaces.[39–42] These capillarity induced aggregates pose a significant barrier to utilizing anisotropic particles to create functional self-assembled materials.[43] Therefore, for creating periodic ordered arrays from shape anisotropic building blocks, it is crucial to reduce this capillary attraction such that it can couple with dipolar interfacial forces (akin to spherical colloids) to dictate the assembly, allowing the anisotropic particles to assemble into their equilibrium configuration. At dilute concentrations, high aspect ratio particles are expected to form an isotropic (I) state at equilibrium. With increasing area fraction, a transition to an equilibrium nematic (N) liquid crystal phase[21] and finally a smectic (Sm) crystal phase[44] is predicted. While numerous theoretical and computational studies have investigated the 2D I–N transition of high aspect ratio particles, experimental validation has been limited to only magnetic ellipsoids under confinement[21] and nanorods at air–water interfaces.[44,45] The assembly of anisotropic particles into these structures may also be important in designing novel materials for liquid crystal thermometers, displays, sensors, and optical electronic devices.[46,47]

Moving from 2D assemblies to three-dimensional (3D) interfacial materials, the mechanical properties of particle-laden fluid interfaces play a crucial role in interfacial stability,[48] which is a prerequisite for arresting the coalescence of droplets and bubbles to form stable Pickering emulsions and foams.[49,50] The high energy penalty associated with creating a droplet interface between two immiscible fluids causes droplet destabilization due to coalescence and Ostwald ripening[51] in the absence of colloidal or surfactant stabilization. The mechanical strength of interfacial colloidal monolayers is dependent on the particle wetting behavior dictated by the position of the three-phase contact line[52] and interparticle repulsive/attractive interactions at fluid interfaces.[53,54] Using silica nanoparticles, Zang *et al.*[55] showed that the maximum compression elastic modulus of monolayers at an air–water interface is higher as particles approach neutral wetting ($\theta_c = 90^\circ$). While repulsive interactions weaken interfacial stability, attractive interactions increase stability, as shown by Elton *et al.*[56] using Janus particles with varying amphiphilicity at an air–water interface. The particle surface wettability and interparticle interactions also impact the resulting collapse mode, *via* either buckling or particle expulsion.[53] In general, monolayers of particles with predominantly repulsive interactions collapse through particle expulsion to the subphase,[53] while particles interacting *via* attractive interactions form monolayers that behave as an elastic sheet that buckles into periodic wrinkles.[53] Both these effects depend on the particle θ_c and interfacial distortion around the particle.[57] Alongside experimental observations, Brownian dynamics simulations suggest that the particle–particle interactions dictate the monolayer collapse mechanism.[58] Since the particle surface roughness and shape anisotropy can induce capillary attraction[36,38] and change the particle pinning behavior,[59] they will naturally impact interfacial stability and collapse.

There are somewhat inconsistent reports in the literature regarding the impact of spherical particle surface roughness on interfacial stability. San Miguel *et al.*[60] reported that emulsion stability increases with particle roughness in the Wenzel wetting regime and decreases with roughness if the wetting occurs in the Cassie–Baxter regime. Mable *et al.*[61] and Van Hooghten *et al.*[40] demonstrated a positive correlation between roughness induced attractive capillary interactions and interfacial moduli, and hence emulsion stability. On the other hand, Kato *et al.*[39] and Elton *et al.*[41] found that the increased roughness on silica nanocolloids decreased the monolayer stability, an apparent contradiction to theoretical prediction of enhanced monolayer elasticity with increased surface roughness.[62,63] Both studies attributed this behavior to structural changes due to frictional contact forces between interlocked surface asperities, a phenomenon which is also responsible for facilitating discontinuous shear thickening in 3D suspensions[64,65] and improving the stability of colloidal gels.[66] While existing literature on both assembly and interfacial stability of rough spherical colloids builds off the fact that roughness induces strong interparticle capillary attraction,[39–41] the situation is clearly more complex and we hypothesize that the impact of particle roughness on interfacial mechanics will depend on the collective contributions of the precise surface roughness magnitude and topography (convex/concave), contact angle, and relative levels of repulsive and attractive interactions at the fluid interface. It is noteworthy that the same capillary-induced kinetic arrest which plagues ordered 2D interfacial assembly of anisotropic particles benefits the use of such particles for 3D interfacial stabilization. For instance, foams and emulsions can be stabilized to a higher degree with fewer ellipsoidal particles[67,68] compared to their spherical counterparts. However, the combined effects of anisotropic particle shape and surface roughness on the mechanics of particle monolayers have not been studied previously.

Engineering particulate interfaces therefore relies on the integration of particle synthesis with well-characterized shape and surface topography, understanding of the single particle interfacial pinning, and examining the resultant multiparticle assembly and interfacial mechanics. Recently, using spheres

and ellipsoids with controlled surface topography and roughness,[69,70] we discovered a paradoxical effect of surface roughness on the pinning and capillary interactions between polymer ellipsoids at fluid interfaces.[43] For spheres, roughness strengthens the interfacial quadrupolar deformation and the corresponding interparticle capillary attraction, in accordance with theory.[38] For ellipsoids, the situation is flipped: increasing roughness reduces the magnitude of the interfacial quadrupolar deformation and the resultant capillary attraction. Based on these singlet and doublet results, we hypothesize that with sufficient roughness-induced decreased capillary attraction, ellipsoids will be able to assemble into ordered monolayers, avoiding capillary driven disordered, kinetically arrested states.

This work aims to test this hypothesis, while also examining more broadly the interfacial assembly and mechanics of rough spherical and ellipsoidal particle monolayers. We measure surface pressure isotherms and observe the resulting microstructures of monolayers of particles with controlled shape, roughness and topography (convex/concave) at an air–water interface. From the surface pressure isotherms, we observe that the roughness-induced change in individual particle pinning and capillary attraction qualitatively translates to monolayers: roughness increases the surface pressure of spherical monolayers but decreases the surface pressure for ellipsoids. However, optical microscopy characterization of the corresponding interfacial microstructures at varying area fraction shows that the magnitude of capillary attraction is not the sole driver of interfacial organization – the particle contact angle and also specific surface topography dictate the monolayer assembly. We observe an I–N phase transition for concave ellipsoidal monolayers, enabling the formation of ordered monolayers at high area fraction. Monolayer interfacial stability and collapse are also dictated by the surface topography. Finally, a qualitative relationship between the observed monolayer morphology and the overall interaction energy landscape is deduced by extracting the free energy per particle from the surface pressure isotherm. Collectively, these results describe how to achieve ordered monolayers comprised of anisotropic particles and more generally control interfacial colloidal assembly with surface topography.

Experimental

Materials

Styrene (Sigma-Aldrich, 99%), azobis(isobutyronitrile) (AIBN, Sigma-Aldrich, 99%), poly(vinylpyrrolidone) (PVP, Sigma-Aldrich, 40 000 g mol^{-1}), isopropyl alcohol (IPA, Fisher Scientific, Certified ACS, $\geq$99.5%), *tert*butyl acrylate (tBA, Aldrich, 98%), 2,2′-azobis(2,4-dimethylvaleronitrile) (Wako V-65, >95%), poly(vinyl alcohol) (PVA, Sigma-Aldrich, 13 000–23 000 g mol^{-1}, 87–89% hydrolyzed), trifluoroacetic acid (TFA, Sigma-Aldrich, 99%), ethanol (EtOH, Fisher Scientific, Certified ACS, 95%), gellan gum (GG, Thermo Scientific), and Sylgard 184 curable silicone elastomer (poly(dimethylsiloxane) (PDMS), Dow Chemical Company) were used as received. Ultrapure deionized water (DI, Millipore Milli-Q) with resistivity >18.2 MΩ-cm was used for preparing aqueous solutions and washing particles.

Particle synthesis and characterization

The library of 10 types of particles studied here is the same as in our previous paper.[43] A detailed description of the particle synthesis protocol and characterization methods can be found there or in the SI. Briefly, smooth linear polystyrene (LPS) spheres are produced by dispersion polymerization (diameter ($2r_0$) = 4 μm). Thermomechanical stretching is used to create ~4.5 : 1 aspect ratio (AR) smooth ellipsoids from the smooth spheres.[70] Convex spheres, which have small circular protrusions (due to poly *tert*butyl acrylate (PtBA) patches) from the surface, are produced with two different roughness *via* seeded emulsion polymerization (SEP). Convex ellipsoids with ~4.5 : 1 AR are produced by thermomechanical stretching of the convex spheres. Concave particles, which have circular/ellipsoidal dimples in the place formerly occupied by the protrusions, are produced from the convex particles *via* acid catalyzed hydrolysis (ACH). ACH washes away PtBA in the form of water-soluble poly(acrylic acid), leaving the surface chemistry of the concave rough particles similar to LPS.[69] Particle size and shape are determined *via* scanning electron microscopy (SEM) and the root-mean-squared roughness is determined by atomic force microscopy (AFM). Previously, we characterized the magnitude of the capillary quadrupole (Δh_{max}) and contact angle (θ_c) of individual particles *in situ* at an air–water interface using Mirau interferometry.[43] A summary of the library of particles synthesized and their individual interfacial characteristics is given in Fig. 1. The particle zeta potential is measured using a Malvern Zetasizer Nano ZSP using particle suspensions of 1 mg mL^{-1} in water in a disposable folded zeta cell.

Surface pressure isotherm measurements

Surface pressure isotherm measurements are performed using a KSV NIMA Langmuir trough (Biolin Scientific) with a glass window. The trough and the platinum Wilhelmy plate are prepared by first cleaning thoroughly with acetone, ethanol and water. The Wilhelmy plate is subsequently placed under flame for a few seconds to dry and remove any remnant contaminants. With the barrier open to a working area of A = 550 cm^2, the trough is filled with 590 mL of water to create a planar air–water interface. The Wilhelmy plate is placed at the middle of the trough and oriented parallel to the barriers to record the surface pressure, $\Pi = \gamma_0 - \gamma$, where γ and γ_0 are the apparent surface tension of the air–water interface with and without the particles, respectively. Before adding particles, the interface is confirmed to be free of surface-active contaminants by compressing the barriers and checking that the surface pressure in the closed-barrier state (A = 35 cm^2) is less than 0.3 mN m^{-1}; otherwise the trough is cleaned again. To prepare monolayers on the water surface, around 25 mg of particles is deposited at the interface from a 4.3 wt% particle dispersion having an equal volume of water and IPA as the spreading solvent.[41,53,54] Before deposition, the particle suspension is sonicated for at least 5 minutes to ensure well-dispersed particles and minimize aggregates. Using a 50 μL Hamilton syringe, the particles are added to the interface by careful drop-by-drop deposition across the entire interface, where

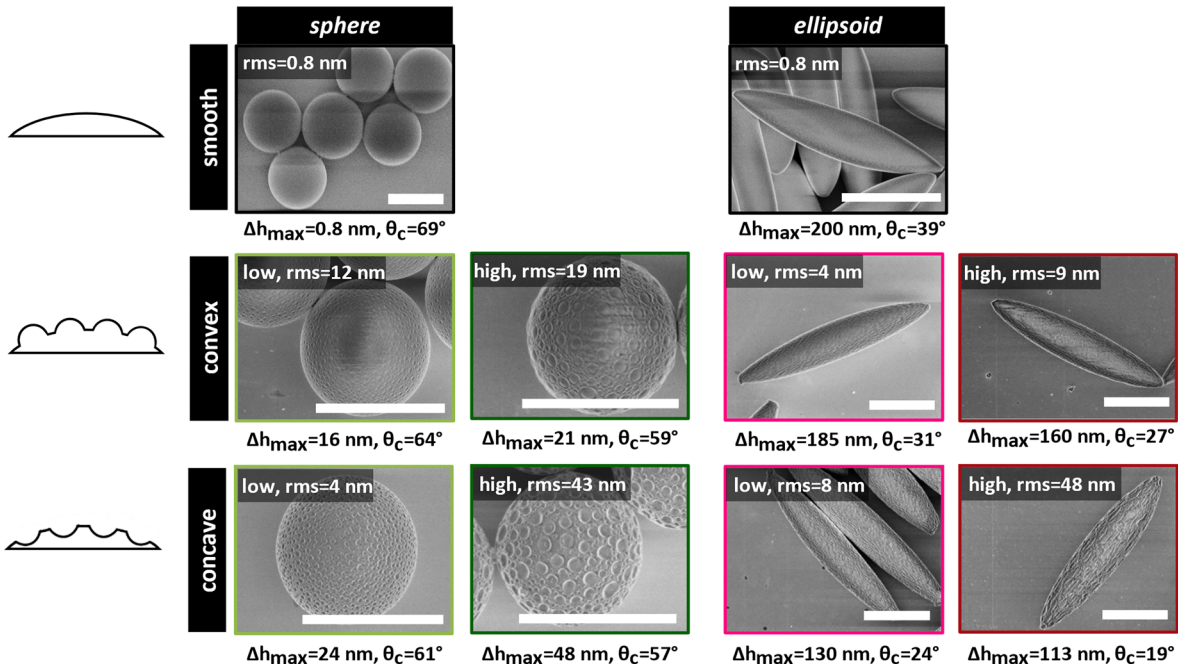

Fig. 1 SEM images along with the corresponding RMS roughness, Δh_{max}, and θ_c values of model smooth (top row), convex (middle row) and concave (bottom row) microspheres and microellipsoids. Ellipsoids have an aspect ratio of $\sim$4.5 : 1. All scale bars represent 5 μm. The left column schematically depicts each type of surface morphology (not drawn to scale).

Marangoni flow helps the particles to spread over the entire water surface. The spreading procedure takes approximately 15 minutes, followed by an additional 30 minutes of waiting time to allow for the complete evaporation of residual IPA[71] before compression. Any residual IPA remaining in the aqueous subphase was measured to have a minimal ($<$0.5%) effect on the air–water interfacial tension. The interface is compressed by two Delrin barriers at 10 mm min^{-1} and the corresponding surface pressure is recorded to yield surface pressure (Π)–area (A) isotherms. We note that in contrast to surfactants, the surface pressure is ill-defined for interfaces with irreversibly adsorbed colloidal particles, so the measured Π can be considered an "apparent" value and we focus on qualitative differences in the magnitude and shape of the isotherms.

The static apparent surface compressibility modulus (ε) is determined from the Π–A isotherm by

$$\varepsilon = -\left(\frac{\partial \Pi}{\partial \ln A}\right)_T \quad (1)$$

It is worth noting that a small shear component develops on a rectangular Langmuir-trough during compression which also induces a change in the shape of the interface. This leads to an extra and deviatoric stress that can either increase or decrease the surface pressure, compared to an isotropic compression on a radial or quadro trough.[72–74] This deviation is more pronounced at higher compression ratios when the interfacial layer starts to become structured and (visco)elastic,[72] *i.e.* close to jamming. Therefore, we attribute the measured ε in this work as "apparent".

Interfacial microscopy and image analysis

To image the monolayer microstructure as it undergoes compression, the trough is mounted on the stage of an upright bright field microscope (Nikon FN1). The stage is covered with a custom-built enclosure to minimize air currents and seated atop a vibration isolation table. All images are captured by a Nikon DS-Fi3 camera with a CMOS image sensor with a 10× objective at 2× zoom in transmission mode.

Microscopy images are processed to reduce noise and thresholded using ImageJ.[75] The resulting black and white images are analyzed by means of in-house codes written in Python. By detecting the pixels at the edges, a least-squares fitting of the contour of the particle is done to extract the centroid coordinates (x_i, y_i) and additionally the orientation (θ_i) of the ellipsoid's major axis. The interfacial particle areal fraction, ϕ, is calculated from the ratio of the total cross-sectional area of particles in the field of view divided by the area of the field of view, $\phi = Na_0/A_m$, where N is the number of particles in the field of view, a_0 is the neutral wetting cross-sectional area of the particles (dimensions obtained from SEM images), and A_m is the microscope view area. Images taken at different barrier positions during compression produced area fractions that are consistent with one another, but less than what would have been predicted based on the amount of particles deposited, indicating some ($\sim$10%) loss to the subphase.

From the particle coordinates, several parameters are calculated to quantify the observed microstructure. The pair correlation function $g(r)$ is calculated from

$$g(r) = \frac{n(r)}{\rho} \quad (2)$$

where $n(r)$ is the number of particles that are within a spherical shell of $r - \mathrm{d}r \leq r \leq r + \mathrm{d}r$ ($\mathrm{d}r$ = 0.21 μm) normalized by the average particle number density, ρ (=N/A_m). For spheres, the 2D hexagonal parameter Ψ_6 of each particle is calculated from the formula

$$\Psi_6 = \frac{1}{n}\left|\sum_{k=1}^{n} \exp(i6\theta_k)\right| \quad (3)$$

where n denotes the number of nearest neighbors and θ_k is the bond angle between the particle of interest and its nearest neighbours. n is calculated by searching for particles within 1.15 times the distance r corresponding to the first peak in $g(r)$. Ψ_6 in the microscopy images is visualized by overlaying the Voronoi diagram (excluding the edges) where the cell colors represent the corresponding particle's Ψ_6.

To quantify the nature of orientation in ellipsoids, the global nematic order parameter,[76] S_2, is characterized using the following equation:

$$S_2 = \langle \cos(2(\theta_i - \theta_2)) \rangle \quad (4)$$

Here, θ_2 is the nematic director that is orthogonal to the direction of interface compression. S_2 ranges from +1 (parallel to the director, θ_2) to −1 (perpendicular to the director), with 0 indicating an isotropic distribution of the particle long axis angles.

To examine the spatial correlation of the ellipsoid's orientation, the angular correlation function $g_2(r)$[77] is calculated as

$$g_2(r) = \langle \cos 2(\Delta\theta_{ij}) \rangle \quad (5)$$

where θ_{ij} is the angle difference between the orientation of two particles i and j within an interparticle separation of $r - \mathrm{d}r \leq r \leq r + \mathrm{d}r$. $g_2(r)$ can assume values from 1 to −1 for particles orientating parallel to perpendicular, with 0 for random alignment. The routines for calculating the above-mentioned parameters are implemented in Python.

Results and discussion

The library of particles studied includes two shapes (sphere/ellipsoid), two topographies (convex/concave), and two levels of roughness magnitude (low/high). Particles are all derived from smooth LPS spheres with a diameter of 4 μm. Convex particles possess PtBA protrusions with controlled geometry (yielding low/high roughness) from either a spherical or ellipsoidal polystyrene particle. ACH removes these protrusions, leaving dimples to produce concave spheres and ellipsoids. All ellipsoids have an AR of ∼4.5 : 1. SEM images of these model colloids along with their corresponding RMS roughness and pinning properties (Δh_{max} and θ_c) from ref. 43 are shown in Fig. 1 and their associated zeta potential values are reported in Fig. S1. From Fig. S1, it can be seen that irrespective of the synthesis condition, there is no significant difference in the surface charge of these model colloids with topography, and only a slight decrease in magnitude from spheres to ellipsoids is observed.

Surface pressure isotherms

To evaluate how surface roughness influences the response of particulate monolayers under compressional deformation, we measured Π–A isotherms of the 10 particle types, deposited and compressed at air–water interfaces using a Langmuir trough. The Π *versus* normalized area (A/A_j) isotherms obtained from spherical and ellipsoidal particles are provided in Fig. 2a and b, respectively. Here, A_j corresponds to the inflection point (maximum in the second derivative) of the Π–A isotherm where the monolayer reaches its maximum packing before jamming[39] in 2D. Compression beyond this point results in the collapse of the particulate layer *via* either buckling, particle expulsion, or multilayer formation.[53,56] The same isotherms in terms of the particle area fraction are given in Fig. 2c and d.

In Fig. 2a, it is apparent that at a given scaled area the surface pressure increases from smooth to concave rough to convex rough spheres. At jamming, there is a marked step-change increase in surface pressure which is less pronounced in the concave spheres, after which the monolayer collapses. The smooth sphere isotherm is in agreement with prior work using spheres synthesized with the

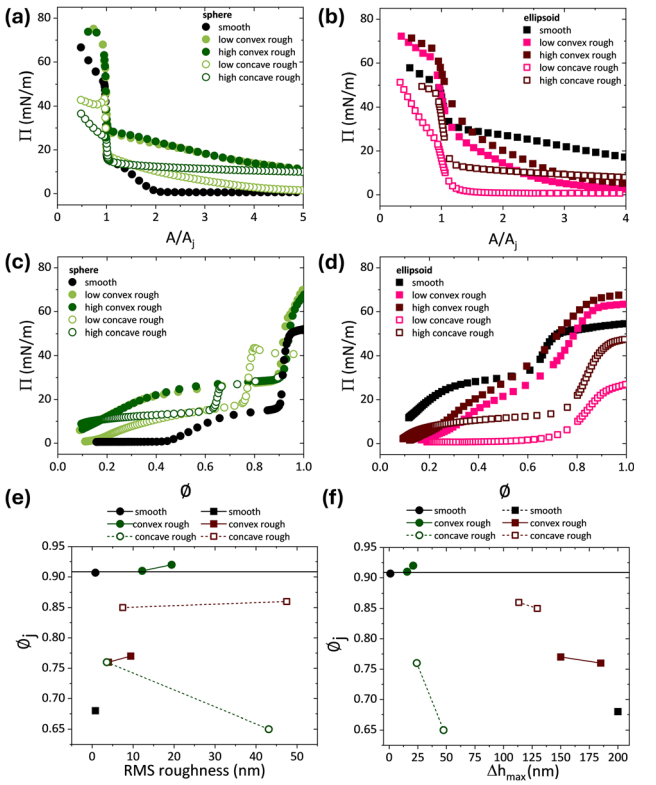

Fig. 2 Surface pressure (Π) isotherm of (a) microspheres and (b) microellipsoids with smooth, convex rough, and concave rough surface morphology as a function of trough area (A) normalized by the area at jamming (A_j). (c) and (d) are the same data scaled by the particle area fraction (ϕ) deduced from optical microscopy measurements. The corresponding particle area fraction at jamming, ϕ_j, for these spheres and ellipsoids as a function of (e) RMS roughness and (f) quadrupolar deformation, Δh_{max}. Here, the horizontal line denotes the maximum achievable packing fraction in 2D. Note that any data point above ϕ_j in (c) and (d) is aphysical and is retained in the graph for visual purposes only.

same AIBN initiator.[78] Here, the surface pressure increases only after the compression overcomes repulsive electrostatic interactions.[79] The rough particles possess added capillary attraction (Δh_{max}),[43] and therefore produce significant surface pressure at higher interfacial areas (lower area fractions), in line with prior work on rough carbon black[40] and rough fumed silica particles.[41] However, in these data, the effect of topography is already apparent: despite overlapping roughness, concave particles possess stronger capillary attraction (measured *via* Δh_{max}), yet have weaker surface pressure. Additionally, from Fig. 2c, it is evident that only the concave particles jam at lower area fractions with increasing roughness.

The Π–A isotherm behavior of ellipsoids (Fig. 2b) is qualitatively opposite to that of spheres, suggesting that the contradictory impact of surface roughness that we originally reported on the single particle interfacial pinning[43] manifests in compressed monolayers as well. Due to the decreased capillary attraction (Δh_{max}), rough ellipsoids in general demonstrate a lower surface pressure than their smooth analogues at a given A/A_j. However, the effect is non-monotonic, with lower surface pressures observed for the particles with lower rms roughness of each topography. Concave ellipsoids were measured to have the weakest capillary attraction, and their isotherm exhibited the largest departure from smooth ellipsoids, in both magnitude and shape. We note that the interfacial behavior of low concave rough ellipsoids resembles hard sphere behavior[78] where the surface pressure is negligible until the particles come into apparent contact at high area fractions, at which point it rises abruptly (Fig. 2d). High concave rough ellipsoids show a similar behavior, but with an offset of around 10 mN m^{-1}. This once again indicates that, apart from particle surface roughness magnitude, surface geometry also plays a crucial role in dictating their interfacial behavior.

Fig. 2e and f show the particle area fraction at jamming, ϕ_j, as a function of roughness and interfacial quadrupolar deformation, respectively. The corresponding surface pressure at jamming and collapse is given in Fig. S2. Smooth and convex spheres jam at area fractions approaching the maximum achievable packing fraction in 2D, 0.907.[78] This value also aligns with that obtained from simple geometric arguments[80] or simulations of jammed disks in 2D.[81] However, despite having Π–A isotherms more similar in shape to smooth spheres, concave spheres jam at much lower area fractions (ϕ_j = 0.65 for the highest roughness/capillarity). On the other hand, smooth ellipsoids jam at ϕ_j = 0.68, which is just below the simulated 2D random close packing (ϕ = 0.7) of AR = 4 ellipses.[82] Unlike spheres, ϕ_j in ellipsoids increases with increasing roughness, with the concave ellipsoids approaching the maximum packing in 2D, which is 0.914 for an

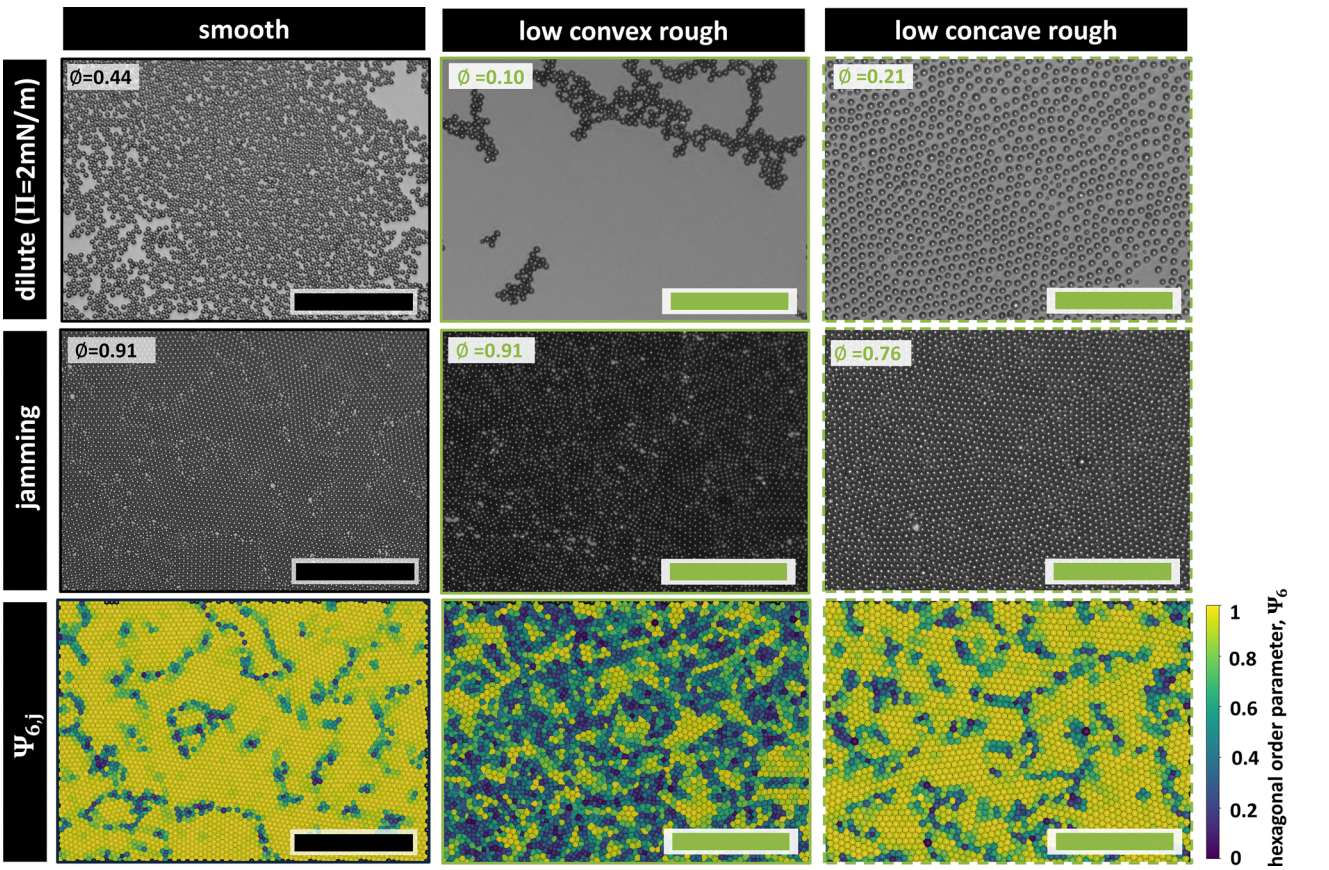

Fig. 3 Optical microscopy images of smooth, low convex, and low concave spheres at an air–water interface at dilute (Π = 2 mN m^{-1}, top row) and jamming (middle row) states in conjunction with the respective particle area fraction (ϕ) at the interface. The bottom row is a Voronoi overlay of the 2D hexagonal order parameter at jamming ($\Psi_{6,j}$). All scale bars represent 100 μm.

AR = 4 ellipsoid. With the exception of convex rough spheres, this contrasting behavior between spheres and ellipsoids is again in line with our single particle results: increased capillary interactions cause particulate monolayers to jam earlier (at lower area fractions). However, the surface geometry and its associated change in pinning, overall interaction, and resultant microstructures also influence the jamming point.

Microstructural behavior at the interface

Fig. 3 shows representative microscopy images for spherical monolayers at low area fraction and at jamming, along with the 2D hexagonal parameter, Ψ_6, of microstructures formed at jamming. In these and all subsequent images, the direction of barrier compression is horizontal. For simplicity, we only discuss the images for convex and concave spheres with low rms roughness; similar results were observed for higher roughness and are included in Fig. S3.

Overall, a striking difference in microstructures is observed among smooth, convex rough, and concave rough spheres. At low Π (2 mN m^{-1}), smooth spheres form nearly close-packed large clusters with high area fraction, in agreement with prior work on smooth polystyrene spheres.[31,54] At the same surface pressure, convex spheres form small aggregated clusters and have much lower ϕ. Concave spheres are in between, exhibiting more isolated particles at intermediate ϕ. With increasing compression, the cluster size of smooth spheres increases and, at jamming, forms a complete monolayer having a 2D maximum packing fraction, ϕ_j = 0.91, as discussed earlier. On the other hand, the individual clusters of convex spheres further aggregate to form a dendritic structure with large voids. At jamming, convex sphere monolayers possess defects in remnant void spaces. However, convex spheres still reach similar area fraction as smooth spheres at jamming, likely due to interlocking asperities and minor out-of-plane movement of the particles. In contrast, the concave particles form a hexagonally ordered monolayer that jams at a decreased area fraction due to increased defects.

To quantify the spherical particle assembly, we calculated $g(r)$ and Ψ_6 as a function of ϕ and topography. Fig. 4a shows $g(r)$ obtained from the analysis of the images at jamming. For smooth and concave spheres, we notice several strong peaks at peak ratios around 1, 1.73, 2, 2.65, and 3, as expected for a hexagonal lattice structure.[83] In the case of convex spheres, the $g(r)$ profile exhibits broad and weak peaks, as expected from the absence of any long-range order. These observations from $g(r)$ at jamming are also shown in the hexagonal order parameter in Fig. 3 (bottom row, also Fig. S4). Although concave spheres form hexagonal monolayers, qualitatively we observe increased grain boundaries and smaller continuous domains of perfect hexagonal order. While the maximum peak for smooth and convex spheres occurs at $r/2r_0$ = 1 (in Fig. 4a), it occurs at a higher surface separation for concave spheres, confirming their increased separation and reduced ϕ_j. A peak just before $r/2r_0$ = 1 in high convex spheres explains the ability of these particles to approach maximum packing at jamming despite disordered assembly due to strong capillary interactions. This is likely due to the protrusions being able to interlock, allowing the particles to pack more closely together. We discuss

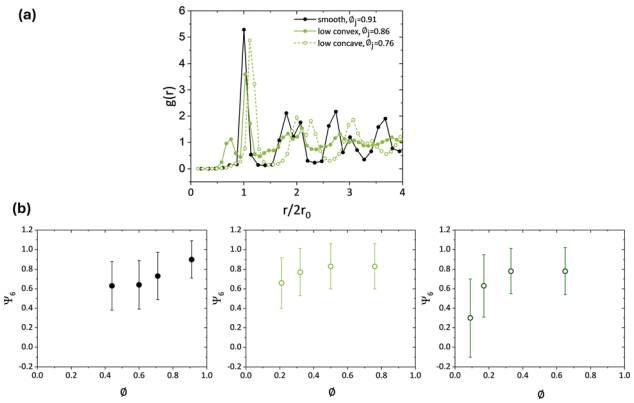

Fig. 4 (a) Radial distribution function, $g(r)$, of smooth, low convex rough, and low concave rough spheres as a function of the particle center-to-center separation distance (r) at their jamming area fraction (ϕ_j). (b) Hexagonal order parameter Ψ_6 of smooth (left), low concave rough (middle), and high concave rough (right) spheres with increasing area fraction ϕ.

how the $g(r)$ profile evolves with ϕ for smooth and concave spheres in the SI (corresponding to Fig. S5) and the associated change in Ψ_6 is shown in Fig. 4b. The uptick in Ψ_6 at lower ϕ for concave spheres compared with smooth spheres results from increased capillary interactions causing assembly at lower area fractions.

Based on the above discussion, we can qualitatively conclude that the microstructures of convex spheres are driven principally from strong attractive interactions due to their increased capillary quadrupole ($\sim 10^3\ k_BT$ at close interparticle separation). We note that since the convex particles have PtBA protrusions, there might be some hydrophobic–hydrophobic attraction between PtBA patches, but these interactions are negligible and occur over a very small distance ($\sim$10 nm)[84,85] compared to long-range capillary attraction. However, despite similar capillarity, concave spheres retain significant repulsive interactions to contribute to their loose yet ordered microstructures. In addition to dipolar repulsion, higher-order multipoles caused by contact line pinning along the sharp ridges of concave particles could also cause *repulsive* capillary interactions in the near-field. This implies that the surface topography plays a pivotal role in dictating the overall interaction and final microstructures, in addition to the altered capillarity by the roughness magnitude.

Analogous to the spherical particles, we optically imaged the monolayers containing ellipsoidal particles of varying surface topography and roughness magnitude to investigate and quantify their structural rearrangement upon interfacial compression or increasing ϕ. Characteristic images of smooth, high convex rough, and high concave rough ellipsoids along with ϕ under dilute (Π = 5 mN m^{-1}) and jamming conditions are given in Fig. 5. For brevity, the high roughness convex and concave ellipsoids are shown in the main text, with the low roughness in Fig. S6.

Soon after deposition, smooth ellipsoids form percolating aggregated networks, where both side-to-side (S–S) and tip-to-tip (T–T) contacts are present. As the compression progresses, space-spanning aggregates become denser, with decreasing

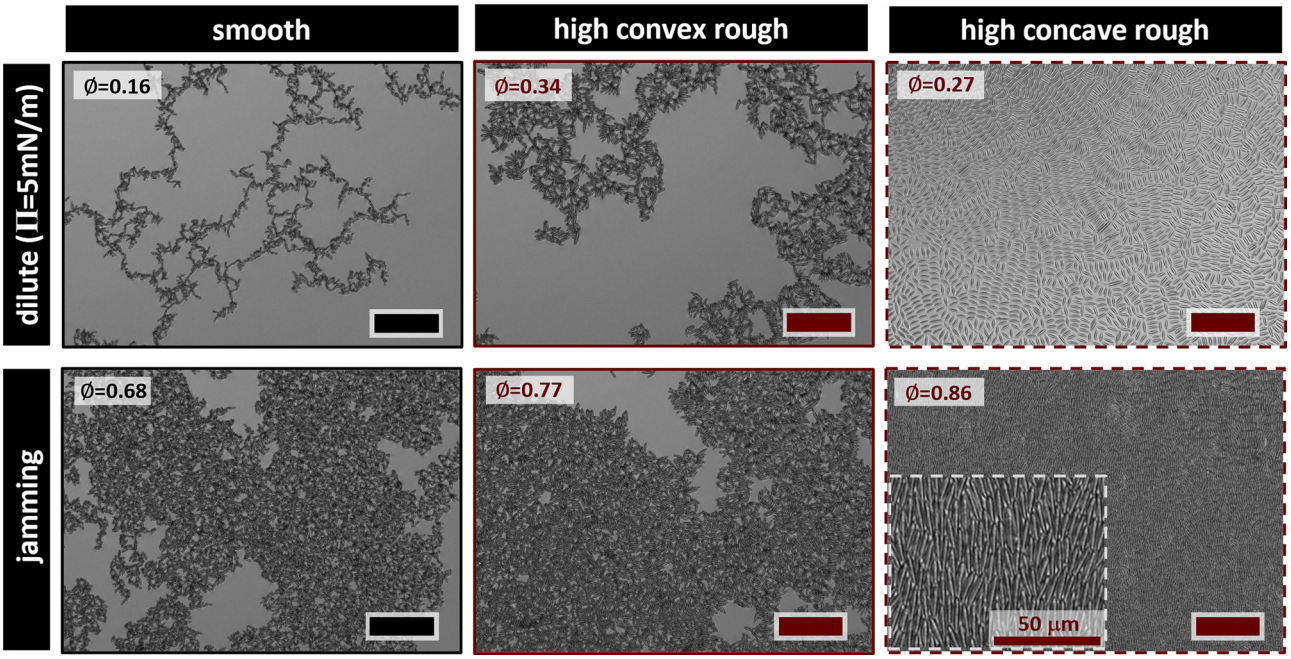

Fig. 5 Optically imaged microstructures at an air–water interface formed by smooth, high convex rough, and high concave rough ellipsoids under dilute (surface pressure, Π = 5 mN m^{-1}) to jamming conditions, combined with the corresponding particle area fraction (ϕ) at the interface. The inset of the bottom-right image shows long-range orientationally ordered high concave rough ellipsoids in the direction perpendicular to the monolayer compression. All scale bars represent 100 μm unless otherwise mentioned.

void fraction, and finally reach a jamming transition at ϕ_j = 0.68. This value is just below the simulated 2D random close packing (ϕ = 0.7) of AR = 4 ellipses.[82] In our case, the smooth ellipsoids jam at a relatively low ϕ due to the disordered aggregated structures as a consequence of lateral capillary attraction between the particles.[36,86] Both low and high convex rough ellipsoids exhibit a similar microstructure progression as smooth ellipsoids, condensing into a disordered monolayer due to dominant attractive interactions. However, convex ellipsoids jam at a higher ϕ which can be attributed to the roughness induced decrease in Δh_{max} as well as associated capillary attraction,[43] as discussed earlier. We suspect that this reduced capillary attraction lowers the energy barrier for additional particle rearrangements to occur on compression, explaining the shift of ϕ_j to higher values for convex ellipsoids.

The microstructures of concave ellipsoids are remarkably different – kinetic arrest is not observed and the particles eventually assemble into dense, orientationally ordered monolayers at close packing. At low surface pressure (*i.e.* at low ϕ), concave ellipsoids do not aggregate; rather they are organized into chains of well separated particles in a predominantly S–S configuration. At this stage, there is no preferential orientation adopted by the chains, which are arranged in different directions with respect to compression and separated by T–T triangles and flower-like T–T defects. This behavior indicates that the roughness induced decrease in capillary attraction is now balanced by the interparticle repulsion, forming a finite separation distance between the concave ellipsoids, similar to the concave spheres. As the interfacial areal density increases, it becomes increasingly difficult for the S–S chains to point in random directions and as the system approaches jamming, they undergo a transition to an ordered anisotropic phase having uniaxial symmetry, with the tips oriented perpendicular to the compression direction. Consequently, concave ellipsoids experienced an even more delayed onset of jamming, reaching ϕ_j = 0.85 and 0.86 for low and high concave ellipsoids, respectively. The combination of interfacial rearrangement and compression to higher area fractions is a consequence of the roughness reducing the capillary attraction to a level sufficient to allow dipolar repulsion to become significant, providing a barrier against the formation of kinetically arrested structures as observed otherwise. While not directly measured here or in our prior interferometry studies, near-field capillary repulsion could also aid in the formation of the observed microstructures. Undulations in the three-phase contact line, as seen here from roughness, can induce multipole orders in U_{cap} at very small distances, making the potential repulsive in the near-field.[38,87] These multipolar interactions are relevant when the separation distance is on the order of particles' characteristic lengths and is dominated by the specifics of the geometry and wetting characteristics of the particle surface.[88] We hypothesize that, regardless of the particle shape, the concave geometry might result in near-field capillary repulsion owing to the mismatch in contact line undulations at the dents between the two interacting particles. For spheres, this could also allow for the retention of some degree of hexagonal ordering despite concave roughness. For ellipsoids, with long-range capillary quadrupolar attraction attenuated, this near-field multipolar repulsion could couple with dipolar repulsion to enable the particles to avoid kinetic arrest and encourage rearrangement into aligned microstructures as the interface is compressed.

To quantify how the ellipsoidal particles arrange as the interface is compressed, we analyzed $g(r)$, S_2, and $g_2(r)$ of the particles as a function of ϕ. To understand this transition, the $g(r)$ progression of high concave rough ellipsoids with ϕ is shown in Fig. 6. At low ϕ (0.16), the first peak is due to S–S organization, with the next peak being the characteristic of T–T "flower-like" or triangular assembly.[89] The peaks at a larger separation distance indicate the T–T orientation of the particles of two parallel chains. The peaks here are rather gradual since the chains are not perfectly parallel to each other. At ϕ = 0.33, the peak corresponding to S–S organization shifts to a lower value as the monolayer compacts. The next peak indicates the formation of S–T arrangements as observed in splay structures[90] at the expense of triangular configuration. This continues at the highest ϕ analyzed (0.49). Here, the peak associated with T–T occurs at a slightly lower r than what would be expected for a perfectly aligned T–T particle with a finite separation distance. This is due to the particles forming zipper teeth[91] like structures upon compaction that reduces the center-to-center distance. A shoulder prior to this peak is an indication of the remnant S–T particles that have not yet aligned in the direction orthogonal to the barrier compression. A similar behavior of $g(r)$ at varying area fraction is observed for monolayers of low concave rough ellipsoids, and hence the results are not included. The $g(r)$ of smooth and convex ellipsoids at ϕ_j is compared in Fig. S7. For these monolayers, only one sharp peak is observed that corresponds to S–S contact. At a larger separation distance, there is no substantial correlation, indicative of the disordered nature of the jammed monolayer.

The nematic order parameter S_2 is an effective parameter to characterize the angular distribution of anisotropically shaped particles relative to a director, θ_2, defined to be perpendicular to the direction of compression. Fig. 7a shows the progress of S_2 for the five different types of ellipsoids with varying ϕ. For smooth and convex ellipsoids, we limit the calculation to only low and high area fraction, and for concave ellipsoids, we conduct the calculation up to ϕ = 0.55, because of the limitations in image analysis. We observe that the S_2 of smooth and convex ellipsoids is near-zero across all area fractions, as expected from the random orientation and isotropic disordered structure observed over the entire interfacial compression. On the other hand, concave ellipsoids increasingly align with the nematic director, undergoing an isotropic–nematic (I–N) transition from ϕ = 0.3 to 0.5. Representative analyzed images showing the development of order are shown in Fig. 7b, which is only improved as the monolayer compacts (see also Fig. 5). Even though the S_2 value is negligible at low ϕ, we can see from Fig. 5 that the S–S chains are aligned along a local director, forming a multi-domain structure with local orientational ordering. With increasing ϕ, the particles align along a global director in order to reduce the free energy of the system. A similar conclusion can be drawn by quantifying $g_2(r)$ and how it changes with ϕ; the findings are discussed in the SI (see associated Fig. S8–S11).

From Fig. 7a, we observe a gradual I–N phase transition, as opposed to the first order transition shown by infinitely thin rods in 3D.[21,92–96] This transition is likely resulting from the

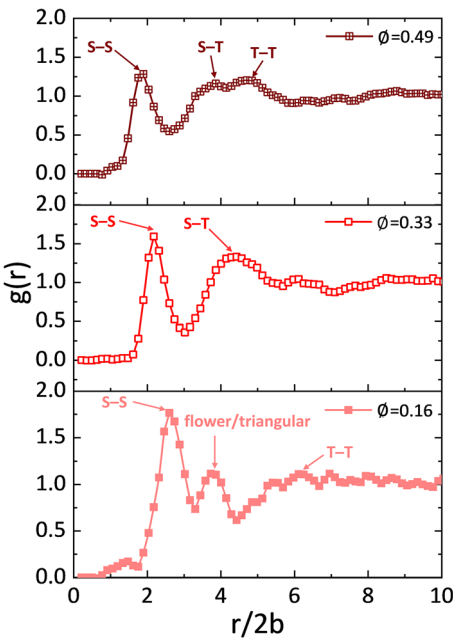

Fig. 6 The change in the radial distribution profile ($g(r)$) of high concave rough ellipsoids as the interface undergoes compression or the particle area fraction (ϕ) increases. The center-to-center separation distance r is normalized by 2b, b being the semi-major axis length of the ellipsoid.

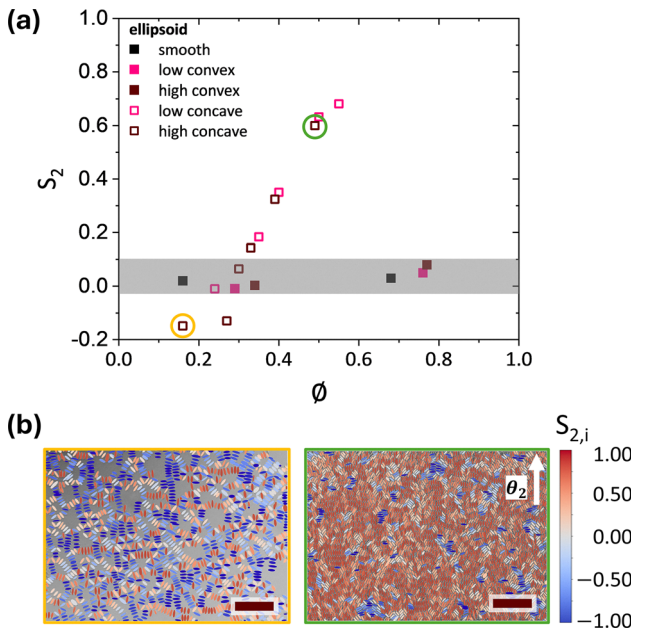

Fig. 7 (a) Nematic order parameter S_2 as a function of the area fraction ϕ for the monolayers of smooth, convex and concave rough ellipsoids. While concave rough ellipsoids exhibit an isotropic-to-nematic (I–N) phase transition, smooth and convex rough ellipsoids remain isotropic (the shaded region) with increasing ϕ. (b) The color-coded overlay of individual particle orientation ($S_{2,i}$) that went into the calculation of S_2 of high concave rough ellipsoids at low and high ϕ as marked by the hollow sphere symbol in (a). A value of $S_{2,i}$ = 1 and −1 indicates that the particles are orientated parallel and perpendicular, respectively, to the director θ_2 which is orthogonal to the compression direction. All scale bars represent 100 μm.

competition between interparticle interactions and configurational entropy of the particles as the interfacial particle areal density increases, as observed in the case of lyotropic liquid crystalline polymers, where monomer density in the solution drives the I–N transition balancing the excluded-volume interactions and the configurational entropy of the macromolecules.[97] Applying an external magnetic field to a colloidal system of AR = 4.9 super-paramagnetic ellipsoidal particles confined between two glass coverslips, Tan *et al.*[21] also reported a continuous 2D I–N phase transition with increasing packing density. Here the authors suggested that the magnetic field contributed to overcoming the local free energy barrier associated with the metastable state to access the thermodynamic ground state (N), resulting in the I–N transition.

Finally, we conclude this section by highlighting the plausible mechanism behind the interfacial 2D I–N phase transition of ellipsoidal particles. Introduction of surface roughness decreases interparticle capillary attraction, which decreases the energy barrier to particle rearrangements and increases the relative importance of dipolar repulsion upon compression. Such existence of an energy barrier between two phases can be visualized by extracting local free energy of the configurations from the distribution of the relative angles ($\Delta\theta$) between anisotropic particles[98] (see SI text for detailed discussion associated with Fig. S12). While the concave ellipsoids studied here have slightly weaker interfacial quadrupolar deformation/capillary attraction than convex ellipsoids, the stark change in interfacial microstructure indicates that concave geometry uniquely contributes to particle self-assembly, perhaps *via* increased dipolar repulsion and near-field capillary repulsion, as discussed earlier. This allows for the avoidance of kinetically arrested states upon particle deposition and subsequent compression, enabling concave ellipsoidal particles to approach their energetically favorable nematic phase.

The non-aggregated packing of the concave ellipsoids soon after deposition at the air–water interface can be derived from the high excluded volume due to their anisotropic shape[99] and decreased capillary attraction now balancing repulsion. At a high compression ratio (*i.e.* at high ϕ), the particles align orthogonal to the compression direction, *i.e.*, parallel to the barrier, forming an *N* phase. This alignment occurs to optimize the entropy of the self-assembled system by minimizing the excluded volume per particle, as first proved by Onsager[96] *via* theoretically treating a system of hard rod colloids. At a given pressure and temperature, all phenomena must seek a state with minimized Gibbs free energy *via* either lowering the enthalpy or raising the entropy, or both.[100] Since our system has seemingly both long-range attraction and repulsion, soon after deposition at low ϕ, the particles arrange solely depending on the energy minimization (balance between reduced capillary attraction and increased dipolar and capillary repulsion) and not entropy maximization as the confinement is not still imposed. Therefore, we see a mixture of S–S and T–T "flower-like" assembly or triangles. At high ϕ, the system will lower the free energy and maximize the free volume by aligning with the barrier at the expense of entropy, when subjected to a lower interfacial area imposed by the barrier compression.

Unlike spheres, the interaction potential between shape anisotropic particles is highly dependent on both their mutual orientation and their interparticle separation. A pair of ellipsoids will minimize their interaction energy *via* lateral association as the overall interaction is minimized in S–S orientation compared to T–T orientation,[42,91] fostering the I–N phase transition. This transition is an indication of the importance of both entropic and energetic contributions to the equilibrium assembly achieved by the concave rough ellipsoids.

Mechanical stability of monolayers

To investigate the effect of topography on monolayer mechanical stability, we calculated the apparent static compressibility (ε) from the Π–A isotherm, which reaches a maximum (ε_{max}) at the jamming point of the isotherm ($A/A_j = 1$). ε_{max} signifies the maximum resistance exhibited by the monolayers to compressive deformation.

Fig. 8a shows ε of each type of sphere as the interface compression progresses. Smooth spheres exhibit the highest apparent compressibility at jamming, with a lower maximum observed for the concave and convex particles in part due to their decreased contact angle (increasing hydrophilicity). For convex spheres, the compressibility is negligible up to a much larger surface pressure. The convex spheres form small locally close-packed, isolated aggregates (as in Fig. 3) due to high capillary attraction that leads to high Π, but since the clusters are well separated the interface cannot resist the deformation, yielding small ε at even higher Π. Once compressed further at high surface pressures, the individual clusters become connected and form a dense continuous structure which is now able to resist compressive deformation.[101] On the other hand, the concave spheres form repulsion dominated non-aggregated structures (as shown in Fig. 3 and discussed in the previous section) at the interface. This may couple with the decreased θ_c, to further decrease the mechanical resistance of the monolayer compared to smooth and convex spheres.

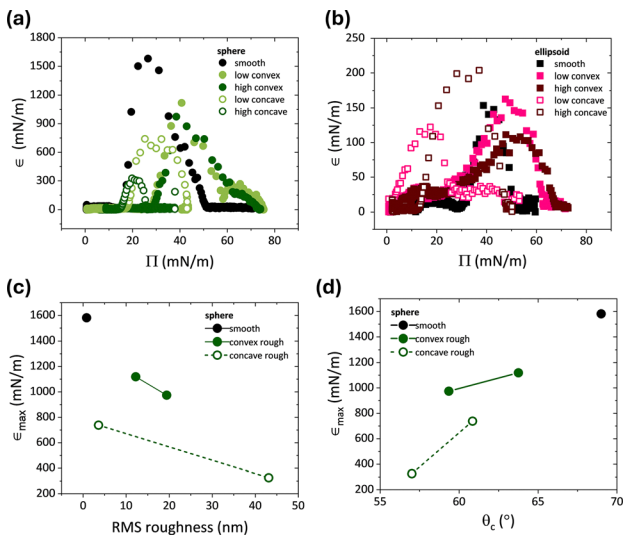

Fig. 8 The progress of surface compressibility modulus ε of (a) spherical and (b) ellipsoidal particles with varying surface topography as the interface is compressed or the surface pressure Π increases. The maximum surface compressibility modulus ε_{max} of spherical particles as a function of their concomitant (c) RMS roughness and (d) contact angle θ_c.

For ellipsoids (Fig. 8b), ε for smooth and convex ellipsoids is negligible up to a very large Π compared to the concave ellipsoids. A similar reasoning that we used for convex spheres can be invoked here, *i.e.*, with increasing compression or increasing ϕ, the area spanning dendritic structures of smooth and convex ellipsoids forms more interconnected networks, which leads to increased resistance to interfacial deformation at high Π. Qualitatively, the concave ellipsoids show a similar behavior as their smooth spherical counterparts, due to the formation of well-separated microstructures.

The behavior of ε_{max} for spherical particles as a function of surface roughness and contact angle is shown in Fig. 8c and d. Overall, with increasing roughness, ε_{max} decreases, *i.e.*, the ability of the interface to resist the compressive deformation reduces. This decrease in interfacial stability is more pronounced for concave particles. In our previous work,[43] we showed that the increase in roughness decreases θ_c (also listed in Fig. 1). Expressing this ε_{max} dependency in terms of the corresponding θ_c (Fig. 8d) shows a linear decay with increasing roughness. We note that a change in wetting behavior also changes the detachment energy, E_{det} (or trapping energy holding the particles at the interface), which seems to have negligible impact compared to particle position on monolayer's mechanical response (see SI for additional discussion on E_{det} associated with Fig. S13). Irrespective of the surface type, ε_{max} of ellipsoids is small compared to spheres, which can be attributed to their decreased θ_c and E_{det}. However, ε_{max} of ellipsoids exhibits a nonmonotonic dependency on particle surface roughness and associated θ_c.

As discussed in the introduction, previous studies show varied and at times conflicting dependence of interfacial stability on particle surface roughness, due to particular properties of the particle/interface under study.[39–41,60,61] Based on our combined results of individual particle pinning and monolayer mechanics, it is apparent that the effect of particle roughness and its type on capillary interaction mediated particle arrangements, frictional contact forces, and changes in microscopic wetting behavior at the fluid interface all play a significant role in stabilizing rough particle laden interface systems. For spheres, roughness increases capillarity, but also causes a decrease in θ_c, which decreases the stability of the interface as particles become more hydrophilic. We hypothesize that if wetting behavior could be controlled independently from surface roughness, for the same wetting behavior, spheres assembled into a loose particulate structure (dominated by repulsion) will show lower stability than the aggregated close-packed structure (dominated by attraction). For a system with similar θ_c and monolayer morphology, the stability could be further governed by the specifics of the particle surface geometry. The higher the interlocking capability, as in convex rather than concave topography, the better potential for the interface to resist mechanical deformation.

The interfacial microstructures and their governing interparticle interactions also dictate how the particulate monolayer collapses after being compressed beyond the jamming point, as confirmed by simulations[58,102] and experiments.[53] It is well established that smooth polystyrene spheres forming a hexagonal close-packed structure collapse *via* buckling instability,[54,79,103] which is consistent with our results. In a similar way, the convex rough spheres undergo out-of-plane deformations after jamming, as can be confirmed from the formation of wrinkles parallel to the barrier as shown in SI Video S1. This behavior can be ascribed to the formation of continuous 2D closely packed structures[103] and the presence of attractive interparticle interactions[53] that arrest the stress relaxation through particle ejection to the subphase. Unlike smooth and convex spheres, the interfacial film of concave spheres collapses *via* particle expulsion to the water subphase, which can be confirmed *via* observing particles floating under the film as shown in SI Video S2. As we discussed earlier, the concave spheres form a loosely packed structure by balancing capillary attraction and dipolar repulsion. Further lateral compression beyond jamming may drive the particles out of this energy minimum and result in increased interparticle repulsion. This increased repulsion with barrier compression can overcome the low E_{det} possessed by these hydrophilic concave spheres, forcing the particles to go into the water subphase.[53] Therefore, the concave spheres show a smaller Π_c compared to smooth and convex spheres (Fig. S2b).

The rough ellipsoids follow the same trend as their corresponding spheres in terms of collapse mechanism and Π_c. The attraction driven continuous particle aggregates observed for smooth and convex rough ellipsoids resist particle displacement from the surface,[101] resulting in monolayer collapse *via* buckling, as shown for smooth ellipsoids in SI Video S3. Monolayers of concave ellipsoids collapse *via* particle rejection to the subphase (SI Video S4), likely due to sufficiently low θ_c and interparticle repulsion favoring desorption of the ellipsoids upon compression beyond jamming.[99] Owing to the same reason, the convex ellipsoids exhibit higher Π_c than concave ellipsoids (Fig. S2d).

Interfacial interaction from the surface pressure isotherm

A quantitative description of how the interparticle interaction energy contributes to the monolayer behavior can also be obtained by calculating the average free energy per particle, $\bar{f}_p$, due to particle interaction, as described by Mears *et al.*[104] This is done by numerically integrating the Π–ϕ isotherm[104] and assuming that the surface pressure is a signature of particle interactions (eqn (6)).[104]

$$\bar{f}_p(\phi) = a_p \int_0^{\phi} \frac{\Pi}{\phi'^2} d\phi' \quad (6)$$

Here, a_p is the cross-sectional area per particle at the interface.

We integrate the Π–ϕ data for both spheres and ellipsoids (as in Fig. 2c and d) starting from $\phi = 0.18$ up to 90% of ϕ_j, since close to jamming, Π is influenced by deviatoric stress.[72] The corresponding results of $\bar{f}_p$ for spheres and ellipsoids as a function of ϕ are shown in Fig. 9a and b, respectively. We see that at a given ϕ, $\bar{f}_p$ qualitatively follows the trend in Δh_{max} and the associated capillary attraction, *i.e.*, increases in rough spheres and decreases in rough ellipsoids. However, the $\bar{f}_p$ of convex spheres is higher than that of high concave spheres, even though Δh_{max} (and the capillary attraction) shows the

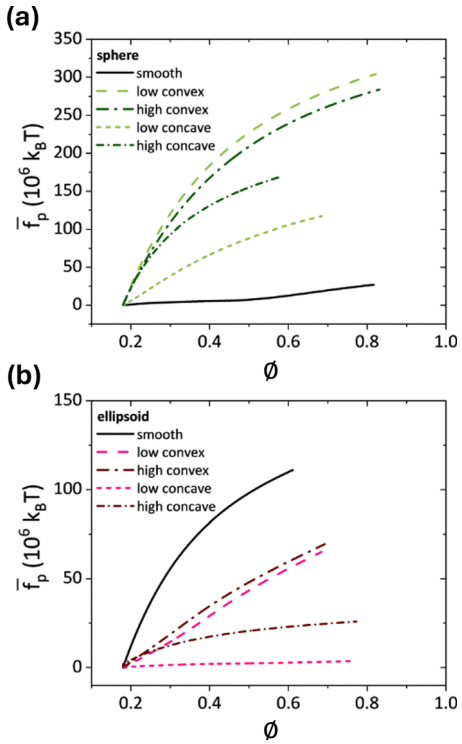

Fig. 9 The interaction energy per particle $\bar{f}_p$ calculated *via* integrating the $\Pi-\phi$ isotherm (Fig. 2c and d) as a function of area fraction ϕ for (a) spheres and (b) ellipsoids with varying surface architecture (smooth, convex, and concave).

opposite trend. We hypothesize that the decrease of $\bar{f}_p$ in concave rough spheres is due to the presence of repulsive interactions as confirmed by isolated microstructures in Fig. 3. On the other hand, the higher $\bar{f}_p$ in convex spheres is due to the dominant capillary attraction, as discussed earlier. A similar analogy holds for the $\bar{f}_p$ behavior of rough ellipsoids. However, since Δh_{max} (and the associated capillary attraction) decreases with increased roughness for concave ellipsoids, one would initially expect the surface pressure (in Fig. 2c) and $\bar{f}_p$ (in Fig. 9b) to likewise decrease with roughness, but our data show the opposite. From our previous work,[43] we note that despite a large increase in roughness (from 7.5 nm to 47.5 nm RMS), concave ellipsoids have a relatively small decrease in Δh_{max} (from 129.5 nm to 113 nm). Collectively, these results demonstrate that the surface pressure isotherm can successfully be used to approximate and interpret particle interactions.

Conclusions

In summary, we have demonstrated that by manipulating interfacial interparticle interactions and wetting behavior *via* particle surface topography and shape, one can control the interfacial organization and mechanical characteristics of colloidal monolayers. Using a Langmuir trough, we measured the surface pressure as a function of particle areal density while simultaneously recording the microstructure *via* optical microscopy at an air–water interface. For a similar particle surface coverage, the measured surface pressure increases in spheres and decreases in ellipsoids with increasing surface roughness. This can be attributed to the associated shape-dependent increase and decrease of long-range capillary attraction between the particles, respectively.

The roughness induced decrease in long-range capillary attraction has substantial impact on the assembly behavior of ellipsoids, particularly those with concave topography. Since the reduced long-range capillary attraction is now comparable to the dipolar repulsion, concave rough ellipsoids form isolated structures avoiding the kinetically arrested assemblies shown by their smooth and convex rough analogues. Because of the isotropic, well-separated structure formed by dilute concave rough ellipsoids, they undergo an interfacial 2D isotropic–nematic phase transition upon compression, forming dense assemblies with long-range orientational order. This minimum energy configuration is unlikely to be achieved by the kinetically arrested ellipsoidal monolayers without external stimuli. Owing to the presence of this alignment, the concave rough ellipsoids can be compressed to a higher degree, forming a denser monolayer and resulting in the delayed onset of jamming compared to their smooth and convex counterparts.

While this study has focused on the behavior of ellipsoids of one AR (4.5), we expect similar behavior for ellipsoids of varying AR. As the aspect ratio increases from the same sized seed particle, shape induced capillary attraction increases, causing a decrease in the monolayer area fraction at jamming. Attenuating capillary attraction *via* surface roughness should likewise increase the jamming point, and for concave ellipsoids the I–N transition is expected to become sharper and move to lower area fractions with increased aspect ratio. However, for very low aspect ratio rough ellipsoids (<2), we expect dipolar repulsion, or near-field capillary multipolar effects, to be an even greater relative contributor to the interparticle potential. In this regime, concave ellipsoids may behave similar to spheres and form stretched hexagonal monolayers at the interface. We look forward to exploring these trends in monolayer assembly as a function of aspect ratio and topography in future work. Likewise, the differences in assembly and jamming between concave and convex rough ellipsoids at similar roughness, capillarity, and aspect ratio point to topographically driven effects. We suspect that incorporating these topographies on colloids of different chemistry (silica and PMMA, for example) would follow similar trends with minor contributions from chemistry-dependent hydrophobic and charge interactions.

Irrespective of the shape of particles, the surface topography-mediated interactions, assembly, and associated wetting behavior of particles dictate the mechanical properties of these particle-laden fluid interfaces. For instance, while monolayer collapse in convex rough particles occurs *via* buckling because of the tangential contact and interlocking in capillary attraction induced close-packed disordered aggregates, for concave rough particles it occurs *via* expulsion to the subphase due to the formation of non-close-packed structures emanating from the balance between capillary attraction and dipolar repulsion. Overall, the findings discussed in this study suggest that particle

surface and shape engineering offers promising routes to tune the mechanical properties of multiphase materials, such as foams and emulsions, and design innovative engineered materials that might emanate from 2D assembly of anisotropic colloidal building blocks at fluid interfaces.

Author contributions

MAR: methodology, formal analysis, investigation, writing – original draft, writing – review & editing, visualization. PJB: conceptualization, funding acquisition, project administration, supervision, writing – original draft, writing – review & editing.

Conflicts of interest

There are no conflicts to declare.

Data availability

The data related to this article has been posted to a publicly accessible database, Open Science Framework (OSF), and can be found here: https://doi.org/10.17605/OSF.IO/YSQDX.

Supplementary information (SI) is available, including additional experimental details, analysis of surface pressure isotherms, microscopy images and characterization (hexagonal order parameter, radial distribution function, angular correlation function), calculations of particle detachment energy, and videos of monolayer collapse. See DOI: https://doi.org/10.1039/d5sm00903k.

Acknowledgements

We acknowledge April Haines (UMass ASCENDS program) for help with the initial Langmuir trough measurements. MAR acknowledges a PPG Fellowship for partial support. Funding for this work was provided by the National Science Foundation under awards no. CBET-2232579 and CBET-2424554.

References

1 T. Ngai and S. A. Bon, *Particle-Stabilized Emulsions and Colloids: Formation and Applications*, The Royal Society of Chemistry, Cambridge, 2014.
2 H. Kumar, M. Tiwari, V. R. Dugyala and M. G. Basavaraj, *Langmuir*, 2023, **40**, 11.
3 S. U. Pickering, *J. Chem. Soc., Trans.*, 1907, **91**, 2001–2021.
4 R. Aveyard, B. P. Binks and J. H. Clint, *Adv. Colloid Interface Sci.*, 2003, **100–102**, 503–546.
5 D. Cai, P. S. Clegg, T. Li, K. A. Rumble and J. W. Tavacoli, *Soft Matter*, 2017, **13**, 4824–4829.
6 M. E. Cates and P. S. Clegg, *Soft Matter*, 2008, **4**, 2132–2138.
7 R. G. Alargova, D. S. Warhadpande, V. N. Paunov and O. D. Velev, *Langmuir*, 2004, **20**, 10371–10374.
8 J. R. Oh, J. H. Moon, S. Yoon, C. R. Park and Y. R. Do, *J. Mater. Chem.*, 2011, **21**, 14167.
9 P. J. Beltramo, D. Schneider, G. Fytas and E. M. Furst, *Phys. Rev. Lett.*, 2014, **113**, 1–5.
10 P. Zheng, M. Li, R. Jurevic, S. K. Cushing, Y. Liu and N. Wu, *Nanoscale*, 2015, **7**, 11005–11012.
11 M. A. Rahman and P. J. Beltramo, *Front. Phys.*, 2023, **11**, 1248706.
12 M. A. Ray, N. Shewmon, S. Bhawalkar, L. Jia, Y. Yang and E. S. Daniels, *Langmuir*, 2009, **25**, 7265–7270.
13 W. Ming, D. Wu, R. Van Benthem and G. De With, *Nano Lett.*, 2005, **5**, 2298–2301.
14 P. Zhang, L. Yang, Q. Li, S. Wu, S. Jia, Z. Li, Z. Zhang and L. Shi, *ACS Appl. Mater. Interfaces*, 2017, **9**, 7648–7657.
15 H. A. Atwater and A. Polman, *Nat. Mater.*, 2010, **9**, 205–213.
16 Z. Cai, Z. Li, S. Ravaine, M. He, Y. Song, Y. Yin, H. Zheng, J. Teng and A. Zhang, *Chem. Soc. Rev.*, 2021, **50**, 5898–5951.
17 C. J. Bettinger, R. Langer and J. T. Borenstein, *Angew. Chem., Int. Ed.*, 2009, **48**, 5406–5415.
18 L. Isa, K. Kumar, M. Müller, J. Grolig, M. Textor and E. Reimhult, *ACS Nano*, 2010, **4**, 5665–5670.
19 O. J. Cayre and V. N. Paunov, *J. Mater. Chem.*, 2004, **14**, 3300–3302.
20 Y. Sun and S. R. Forrest, *J. Appl. Phys.*, 2006, **100**, 073106.
21 X. Tan, Y. Chen, H. Wang, Z. Zhang and X. S. Ling, *Soft Matter*, 2021, **17**, 6001–6005.
22 B. Li, D. Zhou and Y. Han, *Nat. Rev. Mater.*, 2016, **1**(2), 1–13.
23 P. Pieranski, *Phys. Rev. Lett.*, 1980, **45**, 569–572.
24 R. McGorty, J. Fung, D. Kaz and V. N. Manoharan, *Mater. Today*, 2010, **13**, 34–42.
25 D. Wang, H. Duan and H. Möhwald, *Soft Matter*, 2005, **1**, 412.
26 M. E. Leunissen, A. Van Blaaderen, A. D. Hollingsworth, M. T. Sullivan and P. M. Chaikin, *Proc. Natl. Acad. Sci. U. S. A.*, 2007, **104**, 2585–2590.
27 M. G. Nikolaides, A. R. Bausch, M. F. Hsu, A. D. Dinsmore, M. P. Brenner and D. A. Weitz, *Nature*, 2002, **420**, 299–301.
28 R. Aveyard, J. H. Clint, D. Nees and V. N. Paunov, *Langmuir*, 2000, **16**, 1969–1979.
29 X. Xu, Q. Yang, N. Wattanatorn, C. Zhao, N. Chiang, S. J. Jonas and P. S. Weiss, *ACS Nano*, 2017, **11**, 10384–10391.
30 A. Aigner, T. Weber, A. Wester, S. A. Maier and A. Tittl, *Nat. Nanotechnol.*, 2024, **19**(12), 1804–1812.
31 M. Rey, A. D. Law, D. M. A. Buzza and N. Vogel, *J. Am. Chem. Soc.*, 2017, **139**, 17464–17473.
32 M. Grzelczak, J. Vermant, E. M. Furst and L. M. Liz-Marzán, *ACS Nano*, 2010, **4**, 3591–3605.
33 M. Cavallaro, L. Botto, E. P. Lewandowski, M. Wang and K. J. Stebe, *Proc. Natl. Acad. Sci. U. S. A.*, 2011, **108**, 20923–20928.
34 D. Ershov, J. Sprakel, J. Appel, M. A. C. Stuart and J. van der Gucht, *Proc. Natl. Acad. Sci. U. S. A.*, 2013, **110**, 9220–9224.
35 P. Poulin, H. Stark, T. C. Lubensky and D. A. Weitz, *Science*, 1997, **275**, 1770–1773.
36 J. C. Loudet, A. M. Alsayed, J. Zhang and A. G. Yodh, *Phys. Rev. Lett.*, 2005, **94**, 2–5.
37 T. Young, *Philos. Trans. R. Soc. London*, 1805, **95**, 65–87.

38 D. Stamou, C. Duschl and D. Johannsmann, *Phys. Rev. E: Stat. Phys., Plasmas, Fluids, Relat. Interdiscip. Top.*, 2000, **62**, 5263.
39 A. N. Kato, Y. Jiang, W. Chen, R. Seto and T. Li, *J. Colloid Interface Sci.*, 2023, **641**, 492–498.
40 R. Van Hooghten, L. Imperiali, V. Boeckx, R. Sharma and J. Vermant, *Soft Matter*, 2013, **9**, 10791–10798.
41 E. L. Correia, N. Brown, D. V. Papavassiliou and S. Razavi, *Colloids Interfaces*, 2024, **8**, 17.
42 B. Madivala, J. Fransaer and J. Vermant, *Langmuir*, 2009, **25**, 2718–2728.
43 M. A. Rahman and P. J. Beltramo, *ACS Appl. Mater. Interfaces*, 2024, **16**, 35834–35840.
44 F. Kim, S. Kwan, J. Akana and P. Yang, *J. Am. Chem. Soc.*, 2001, **123**, 4360–4361.
45 M. P. Shortell, H. W. Liu, H. Zhu, E. A. Jaatinen and E. R. Waclawik, *Langmuir*, 2010, **26**, 14472–14478.
46 X. C. Luu, J. Yu and A. Striolo, *J. Phys. Chem. B*, 2013, **117**, 13922–13929.
47 L. Isa, J.-M. Jung and R. Mezzenga, *Soft Matter*, 2011, **7**, 8127.
48 B. Wang, M. Wang, H. Zhang, N. S. Sobal, W. Tong, C. Gao, Y. Wang, M. Giersig, D. Wang, H. Möhwald, S. S. Adkins, D. Gohil, J. L. Dickson, S. E. Webber, K. P. Johnston, M. P. Boneva, N. C. Christov, K. D. Danov, P. A. Kralchevsky, C. C. Monteux, J. Kirkwood, H. Xu, E. Jung and G. G. Fuller, *Phys. Chem. Chem. Phys.*, 2007, **9**, 6344–6350.
49 I. Blute, R. J. Pugh, J. van de Pas and I. Callaghan, *J. Colloid Interface Sci.*, 2009, **336**, 584–591.
50 I. Blute, R. J. Pugh, J. van de Pas and I. Callaghan, *J. Colloid Interface Sci.*, 2007, **313**, 645–655.
51 O. S. Deshmukh, D. Van Den Ende, M. C. Stuart, F. Mugele and M. H. G. Duits, *Adv. Colloid Interface Sci.*, 2015, **222**, 215–217.
52 P. Finkle, H. D. Draper and J. H. Hildebrand, *J. Am. Chem. Soc.*, 1923, **45**, 2780–2788.
53 S. Razavi, K. D. Cao, B. Lin, K. Yee, C. Lee, R. S. Tu and I. Kretzschmar, *Langmuir*, 2015, **16**, 28.
54 J. Lenis, S. Razavi, K. D. Cao, B. Lin, K. Y. C. Lee, R. S. Tu and I. Kretzschmar, *J. Am. Chem. Soc.*, 2015, **137**, 15370–15373.
55 D. Y. Zang, E. Rio, G. Delon, D. Langevin, B. Wei and B. P. Binks, *Mol. Phys.*, 2011, **109**, 1057–1066.
56 E. L. Correia and S. Razavi, *AIChE J.*, 2023, **69**, e18241.
57 I. B. Liu, N. Sharifi-Mood and K. J. Stebe, *Annu. Rev. Condens. Matter Phys.*, 2018, **9**, 283–305.
58 L. A. Pugnaloni, R. Ettelaie and E. Dickinson, *J. Colloid Interface Sci.*, 2005, **287**, 401–414.
59 M. Zanini, C. Marschelke, S. E. Anachkov, E. Marini, A. Synytska and L. Isa, *Nat. Commun.*, 2017, **8**, 1–9.
60 A. San-Miguel and S. H. Behrens, *Langmuir*, 2012, **28**, 12038–12043.
61 C. J. Mable, N. J. Warren, K. L. Thompson, O. O. Mykhaylyk and S. P. Armes, *Chem. Sci.*, 2015, **6**, 6179–6188.
62 J. Lucassen, *Colloids Surf.*, 1992, **65**, 131–137.
63 K. D. Danov, P. A. Kralchevsky, B. N. Naydenov and G. Brenn, *J. Colloid Interface Sci.*, 2005, **287**, 121–134.
64 C. P. Hsu, S. N. Ramakrishna, M. Zanini, N. D. Spencer and L. Isa, *Proc. Natl. Acad. Sci. U. S. A.*, 2018, **115**, 5117–5122.
65 S. Pradeep, M. Nabizadeh, A. R. Jacob, S. Jamali and L. C. Hsiao, *Phys. Rev. Lett.*, 2021, **127**, 158002.
66 F. J. Müller, K. Yang, L. Isa and J. Vermant, *J. Colloid Interface Sci.*, 2025, **690**, 137274.
67 P. J. Beltramo, M. Gupta, A. Alicke, I. Liascukiene, D. Z. Gunes, C. N. Baroud and J. Vermant, *Proc. Natl. Acad. Sci. U. S. A.*, 2017, **114**, 201705181.
68 B. Madivala, S. Vandebril, J. Fransaer and J. Vermant, *Soft Matter*, 2009, **5**, 1717–1727.
69 M. A. Rahman, T. Turner, H. S. C. Hamilton, L. C. Bradley and P. J. Beltramo, *J. Colloid Interface Sci.*, 2023, **652**, 82–94.
70 S. Trevenen and P. J. Beltramo, *J. Colloid Interface Sci.*, 2021, **583**, 385–393.
71 A. Alicke, L. Stricker and J. Vermant, *J. Colloid Interface Sci.*, 2023, **652**, 317–328.
72 M. Pepicelli, T. Verwijlen, T. A. Tervoort and J. Vermant, *Soft Matter*, 2017, **13**, 5977–5990.
73 Y. S. Tein, B. R. Thompson, C. Majkrzak, B. Maranville, D. Renggli, J. Vermant and N. J. Wagner, *Rev. Sci. Instrum.*, 2022, **93**, 93903.
74 S. K. Kale, A. J. Cope, D. M. Goggin and J. R. Samaniuk, *J. Colloid Interface Sci.*, 2021, **582**, 1085–1098.
75 J. Schindelin, I. Arganda-Carreras, E. Frise, V. Kaynig, M. Longair, T. Pietzsch, S. Preibisch, C. Rueden, S. Saalfeld, B. Schmid, J. Y. Tinevez, D. J. White, V. Hartenstein, K. Eliceiri, P. Tomancak and A. Cardona, *Nat. Methods*, 2012, **9**(7), 676–682.
76 J. Vieillard-Baron and M. Carlo, *J. Chem. Phys.*, 1972, **56**, 4729–4744.
77 D. Frenkel and R. Eppenga, *Phys. Rev. A*, 1985, **31**, 1776.
78 M. G. Basavaraj, G. G. Fuller, J. Fransaer and J. Vermant, *Langmuir*, 2006, **22**, 6605–6612.
79 A. G. Bykov, B. A. Noskov, G. Loglio, V. V. Lyadinskaya and R. Miller, *Soft Matter*, 2014, **10**, 6499–6505.
80 J. Pach and P. Agarwal, *Combinatorial Geometry*, Wiley-Interscience, New York, 1995.
81 A. Donev, S. Torquato, F. H. Stillinger and R. Connelly, *J. Appl. Phys.*, 2004, **95**, 989–999.
82 B. J. Buchalter and R. M. Bradley, *Phys. Rev. A*, 1992, **46**, 3046.
83 J. M. Prisaznuk, P. Huang, X. Yong and P. R. Chiarot, *Langmuir*, 2023, **39**, 469–477.
84 Z. Hórvölgyi, S. Németh and J. H. Fendler, *Colloids Surf., A*, 1993, **71**, 327–335.
85 F. Martínez-López, M. A. Cabrerizo-Vílchez and R. Hidalgo-Álvarez, *J. Colloid Interface Sci.*, 2000, **232**, 303–310.
86 H. Lehle, E. Noruzifar and M. Oettel, *Eur. Phys. J. E: Soft Matter Biol. Phys.*, 2008, **26**, 151–160.
87 K. D. Danov and P. A. Kralchevsky, *Adv. Colloid Interface Sci.*, 2010, **154**, 91–103.
88 L. Yao, L. Botto, J. Marcello Cavallaro, B. J. Bleier, V. Garbin and K. J. Stebe, *Soft Matter*, 2013, **9**, 779–786.
89 J. Eatson, S. Bauernfeind, B. Midtvedt, A. Ciarlo, J. Menath, G. Pesce, A. B. Schofield, G. Volpe, P. S. Clegg, N. Vogel, D. M. A. Buzza and M. Rey, *J. Colloid Interface Sci.*, 2025, **683**, 435–446.

90 Z. Zheng, R. Ni, F. Wang, M. Dijkstra, Y. Wang and Y. Han, *Nat. Commun.*, 2014, **5**, 3829.
91 A. M. Luo, J. Vermant, P. Ilg, Z. Zhang and L. M. C. Sagis, *J. Colloid Interface Sci.*, 2019, **534**, 205–214.
92 J. A. Cuesta and D. Frenkel, *Phys. Rev. A*, 1990, **42**, 2126.
93 J. Xia and Y. Han, *Phys. Rev. Res.*, 2024, **6**, 033232.
94 I. Dierking, M. Mitov and M. A. Osipov, *Soft Matter*, 2015, **11**, 819–837.
95 R. Repnik, L. Mathelitsch, M. Svetec and S. Kralj, *Eur. J. Phys.*, 2003, **24**, 481.
96 L. Onsager, *Ann. N. Y. Acad. Sci.*, 1949, **51**, 627–659.
97 S. A. Egorov, A. Milchev, P. Virnau and K. Binder, *Soft Matter*, 2016, **12**, 4944–4959.
98 X. Liu, H. Wang, Z. Zhang, J. M. Kosterlitz and X. S. Ling, *New J. Phys.*, 2020, **22**, 103066.
99 P. Bertsch, M. Diener, J. Adamcik, N. Scheuble, T. Geue, R. Mezzenga and P. Fischer, *Langmuir*, 2018, **34**, 15195–15202.
100 C. G. De Kruif and R. Tuinier, *Food Hydrocolloids*, 2001, **15**, 555–563.
101 A. G. Bykov, G. Gochev, G. Loglio, R. Miller, A. K. Panda and B. A. Noskov, *Colloids Surf., A*, 2017, **521**, 239–246.
102 L. A. Pugnaloni, R. Ettelaie and E. Dickinson, *Langmuir*, 2004, **20**, 6096–6099.
103 A. G. Bykov, G. Loglio, R. Miller and B. A. Noskov, *Colloids Surf., A*, 2015, **485**, 42–48.
104 R. Mears, I. Muntz and J. H. J. Thijssen, *Soft Matter*, 2020, **16**, 9347–9356.